Monthly Notices
of the
ROYAL ASTRONOMICAL SOCIETY

MNRAS **462,** S33–S44 (2016)
Advance Access publication 2016 August 16

doi:10.1093/mnras/stw2046

Observations of high-plasma density region in the inner coma of 67P/Churyumov–Gerasimenko during early activity

Lei Yang,[1⋆] J. J. P. Paulsson,[1] C. Simon Wedlund,[1⋆] E. Odelstad,[2] N. J. T. Edberg,[2] C. Koenders,[3] A. I. Eriksson[2] and W. J. Miloch[1⋆]

[1] *Department of Physics, University of Oslo, Sem Sælands vei 24, postbox 1048, 0317Oslo, Norway*
[2] *Swedish Institute of Space Physics, Lägerhyddsvägen 1, SE-751 21 Uppsala, Sweden*
[3] *Institut für Geophysik und extraterrestrische Physik, Technische Universität Braunschweig, Mendelssohnstraße 3, D-38106 Braunschweig, Germany*

Accepted 2016 August 11. Received 2016 August 9; in original form 2016 June 29

ABSTRACT

In 2014 September, as Rosetta transitioned to close bound orbits at 30 km from comet 67P/Churyumov–Gerasimenko, the Rosetta Plasma Consortium Langmuir probe (RPC-LAP) data showed large systematic fluctuations in both the spacecraft potential and the collected currents. We analyse the potential bias sweeps from RPC-LAP, from which we extract three sets of parameters: (1) knee potential, that we relate to the spacecraft potential, (2) the ion attraction current, which is composed of the photoelectron emission current from the probe as well as contributions from local ions, secondary emission, and low-energy electrons, and (3) an electron current whose variation is, in turn, an estimate of the electron density variation. We study the evolution of these parameters between 4 and 3.2 au in heliocentric and cometocentric frames. We find on September 9 a transition into a high-density plasma region characterized by increased knee potential fluctuations and plasma currents to the probe. In conjunction with previous studies, the early cometary plasma can be seen as composed of two regions: an outer region characterized by solar wind plasma, and small quantities of pick-up ions, and an inner region with enhanced plasma densities. This conclusion is in agreement with other RPC instruments such as RPC-MAG, RPC-IES and RPC-ICA, and numerical simulations.

Key words: plasmas – instrumentation: miscellaneous – methods: data analysis – comets: individual: 67P/C-G.

1 INTRODUCTION

In 2014 August, the European Space Agency Rosetta mission (Glassmeier et al. 2007a) arrived in the vicinity of Jupiter-family comet 67P/Churyumov–Gerasimenko (67P), giving for the first time the possibility to examine *in situ* the evolution of the cometary plasma environment on its path around the Sun. The plasma environment of a comet varies strongly in the course of its highly eccentric orbit (e.g. the aphelion distance of comet 67P is 5.68 au from the Sun, while perihelion is at 1.24 au). On a comet's journey from aphelion towards perihelion, the solar wind and EUV radiation from the Sun are the main drivers of cometary activity and development of plasma structures (Coates 1997). Cometary plasma structures observed by previous missions, e.g. Mach cone, bow shock, cometopause, ion pile-up region and diamagnetic cavity for Jupiter-family comets, such as 67P, are described in more detail in Coates & Jones (2009). These structures are also modelled in state-of-the-art simulations (e.g. Hansen et al. 2007; Koenders et al. 2013; Rubin et al. 2014). In contrast to previous cometary missions [Giotto, International Cometary Explorer (ICE), see e.g. Coates 1997; Coates & Jones 2009] which were fly-bys providing static snapshots of the comet's plasma environment, Rosetta, using a set of instruments dedicated to study the neutral gas and plasma, offers a unique possibility to characterize the dynamics and evolution of cometary plasma structures. However, 67P is a weakly outgassing comet, with a water production rate at perihelion of $Q \sim 10^{27}$–$10^{28}\mathrm{s}^{-1}$ (Snodgrass et al. 2013; Simon Wedlund et al. 2016), which is one to two orders of magnitude smaller than the corresponding outgassing rate for comet 1P/Halley (Combi & Feldman 1993). Thus, the typical structures seen with Giotto for 1P/Halley are expected to be less pronounced or even absent in Rosetta's observations, as shown in recent numerical simulation results (Rubin et al. 2014). However, 67P has displayed, even in the early phase of the mission, a rich and dynamic plasma environment, that was not expected for such a weakly outgassing body (e.g. Clark et al. 2015).

Between 2014 August and September, a set of five instruments as part of the Rosetta Plasma Consortium (RPC; Carr et al. 2007),

⋆ E-mail: lei.yang@fys.uio.no (LY); c.s.wedlund@fys.uio.no (CSW); w.j.miloch@fys.uio.no (WJM)

specializing in the study of the plasma environment, started *in situ* measurements of the low-activity coma, the closest to a comet's aphelion ever made. The Ion Composition Analyser (RPC-ICA), which is a top-hat ion spectrometer (Nilsson et al. 2007), detected the first signatures of H_3O^+ and/or O^+ on 2014 August 7, when Rosetta was 100 km from 67P's nucleus and at a heliocentric distance $R_h \sim 3.6$ au (Nilsson et al. 2015a). On 2014 August 19, the Ion and Electron Sensor (RPC-IES; Burch et al. 2015), which can measure both electron and ion fluxes from 1 eV q^{-1} to 22 keV q^{-1}, found low-energy water-group ions in the energy range 4–10 eV (Goldstein et al. 2015) that they interpreted as ions in the process of being picked up by the solar wind convection electric field. Subsequent observations by RPC-ICA showed enhanced pick-up ion activity at higher energies on 2014 September 21 (Nilsson et al. 2015a) at about 28 km from the comet. In parallel, Clark et al. (2015) observed with RPC-IES a somewhat progressive increase in suprathermal electron fluxes and energies during 2014 August and September. Finally, the fluxgate magnetometer RPC-MAG (Glassmeier et al. 2007b) observed increasing wave activity in the beginning of August with a distinct low-frequency peak at 40 mHz: they tentatively attributed these waves to cross-field currents associated with newly born cometary ions that did not have the time to be accelerated by the solar wind convection electric field (Richter et al. 2015).

Other RPC instruments, i.e. the Langmuir probe (RPC-LAP; Eriksson et al. 2007), and the mutual impedance probe (RPC-MIP; Trotignon et al. 2007) can provide a more complete picture of this increasing cometary activity. In particular, RPC-LAP, consisting of two Langmuir probes collecting electric currents due to the local plasma environment, provides almost continuous measurements of plasma parameters (Eriksson et al. 2007). Using RPC-LAP, the spacecraft potential was seen to regularly go negative from 2014 September to 2015 March (Odelstad et al. 2015). Edberg et al. (2015) subsequently concluded that in 2014 October, low-energy plasma arose mainly from local ionization (photon and electron impact) of the neutral atmosphere of the comet. In their study, they did not find evidence of formation of any plasma boundary due to interaction with the solar wind in the early activity time period. The characteristics of the increasing cometary plasma activity during Rosetta's approach to the comet 67P still remains an open question. In particular, the evolution of cometary ions and high-energy electrons should be considered in detail, as it can provide a better perspective on the evolution of the comet's environment and on the measurements by other instruments. In this paper, in order to address the question of the evolution of the cometary plasma environment, we systematically analyse RPC-LAP data from 2014 May through October during Rosetta's approach to comet 67P. We focus on the increase of the local plasma density and entry into the high-density region (HDR) close to the comet, which we investigate by studying photoelectron emission and other currents to the probe together with the spacecraft potential. Fig. 1 shows the corresponding trajectory of Rosetta around 67P in comet solar orbital (CSO) coordinates ($+x$-axis is in the direction towards the Sun, z-axis normal to the comet orbital plane), between the initial approach in 2014 August, to the bound orbits close to the nucleus from 2014 mid-September through October 15. This approximately corresponds to the period of time which we refer to as the early activity of 67P.

This paper is organized as follows: in Section 2, we explain how the RPC-LAP data sets are analysed, and how different plasma contributions to the probe current are separated. The results are presented in Section 3, where observations are divided into two main physical regions with respect to 67P's early activity. Section 4 presents a discussion of the results in the context of other Rosetta observations in the same range of solar distance R_h. Possible effects of solar radiation fluctuations and different transient events, such as coronal mass ejections (CMEs; McKenna-Lawlor et al. 2016) are also considered.

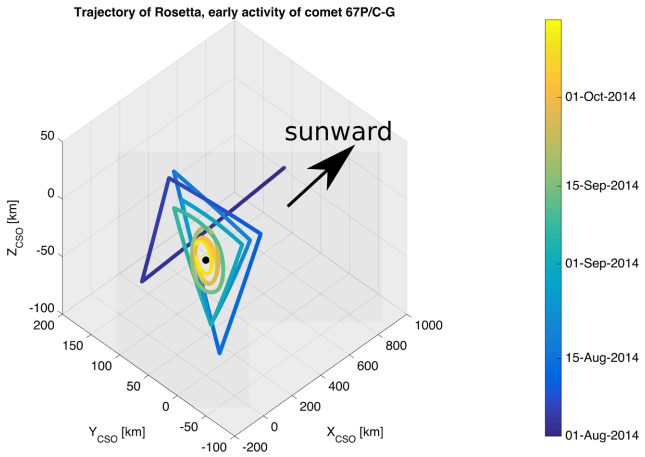

Figure 1. The trajectory of Rosetta between 2014 August and mid-October in CSO coordinates. During 2014 September, Rosetta exited triangular orbits and entered bound orbits close to the nucleus of 67P. The comet's nucleus is located at coordinates (0,0,0), represented by a black sphere. The Rosetta's trajectory is colour-coded according to time.

2 METHODS

In this study, we use the Langmuir probe experiment RPC-LAP onboard Rosetta. We analyse data from probe 1 (RPC-LAP1), which is the probe usually best positioned with respect to the nucleus, and with most stable illumination conditions. RPC-LAP1 is a conducting sphere of radius 2.5 cm, placed on a boom extending 2.24 m from the spacecraft (Eriksson et al. 2007). RPC-LAP performs potential bias sweeps, varying the probe-to-spacecraft potential and collecting the current response. From the resulting current–voltage (I–V) characteristics, one can derive plasma parameters (Schott 1968). In the following section, we will study the current response of the probe and how it relates to photoelectron emission, plasma densities, and spacecraft potential ($V_{s/c}$), which we derive from potential bias sweeps. The details of the analysis and the corresponding theory are discussed in the Appendix. Here we provide only a general description of the approach.

Fig. 2 shows a typical I–V characteristics from RPC-LAP1 (open circles), measured on 2014 September 1, at a distance of 3.5 au from the Sun, during sunlit conditions. The solid line corresponds to the smoothed current. In this figure, we emphasize three regions: (1) ion attraction, (2) electron retardation and (3) electron attraction regions. We use here the convention that electron (ion) current is positive (negative). In the electron retardation region, the probe's potential already attracts ions and starts to repel electrons. However, because of the high velocity of electrons with respect to ions, the electron current might still dominate over the ion current / can be significant until we reach more negative potentials. The point of inflection between the regions in the I–V characteristics is known as the knee potential, V_k, whose location is shown by the solid vertical blue line in Fig. 2. Immediately to the left of V_k, low-energy electrons start to be shielded (with respect to the spacecraft) away from the probe surface, while for lower bias potentials, V_b, an ion-attractive Debye sheath forms around the probe. The slope

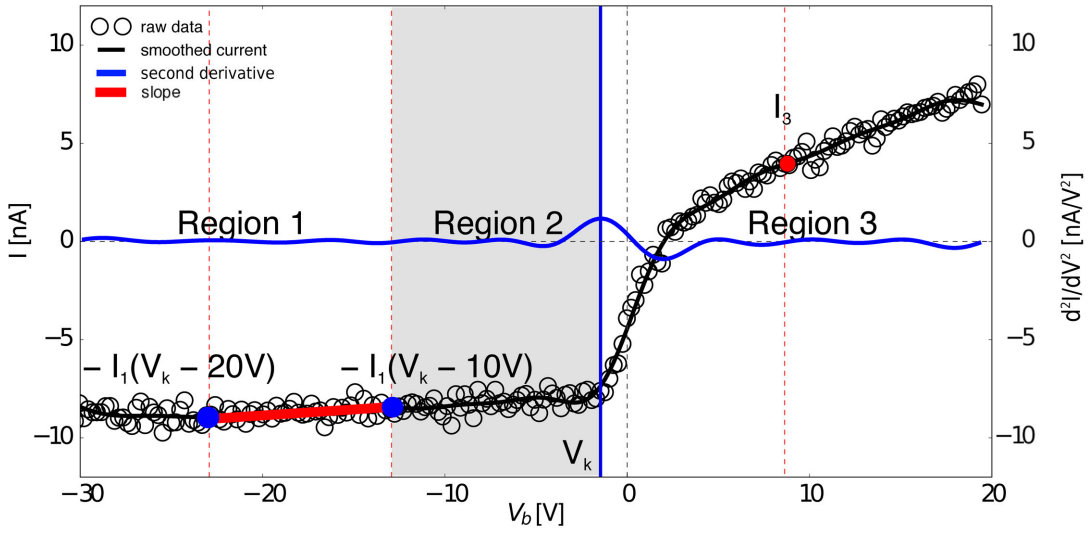

Figure 2. Example of the *I–V* characteristics for RPC-LAP1 during sunlit conditions, measured on 2014 September 1, at distance of 3.5 au from the Sun. The current received by RPC-LAP1, in units of (nA), is shown against the bias potential V_b of the potential bias sweep. The open circles show the collected current, while the solid black line shows the smoothed fit through these data points. The blue vertical line denotes V_k, which, in this case, is negative (corresponding to a positive spacecraft potential $V_{s/c}$). Three regions of the *I–V* characteristics are emphasized: (1) ion attraction (current I_1), (2) electron retardation, and (3) electron attraction (current I_3). The red circle corresponds to current I_3, which is evaluated at the same distance away from V_k, regardless of the probe mode. Its variation over time is an estimate of electron density fluctuations. We take a linear fit through the solid red line and take current I_1 at the intersection of this line with the blue vertical line at V_k. The blue curve shows the second derivative of the fit, whence the position of V_k is found. The second derivative is presented in units of (nA/V^2), as shown on the *y*-axis on the right.

of the red curve in the ion attraction part with the blue vertical line at V_k is the result of competing low-energy electrons that bleed in from the electron attraction region on one hand, and local ions that are accelerated towards the probe, as well as secondary emission associated with high-energy electrons (Garnier et al. 2013) on the other hand.

Several physical processes will be reflected in the RPC-LAP measured currents. First, prior to the initial bound orbit in 2014 September, radiation from the Sun, especially in the EUV part of the spectrum (e.g. Brace, Hoegy & Theis 1988; Huebner & Mukherjee 2015), continuously photoionized the sunlit sections of Rosetta's coating, and as a result, the spacecraft was positively charged. The LAPs also emit photoelectrons when illuminated, and the current in the ion-attractive part of the *I–V* characteristics, where the photoelectrons may escape from the probe, is expected to be proportional to the solar EUV flux. Thus, the photoelectron emission current, denoted I_{ph}, measured by RPC-LAP during sunlit conditions should follow the scaling relation for flux dilution in vacuum,

$$I_{ph} \propto \Psi_{h\nu} \propto R_h^{-2}, \quad (1)$$

where $\Psi_{h\nu}$ is the photon flux from the Sun, and R_h is the heliocentric distance to Rosetta. Eriksson & Winkler (2007) verified this relation for Langmuir probes in space by comparing photoelectron measurements on the Cluster satellites with solar EUV data from TIMED/SEE for the years 2003–2006.

Secondly, as Rosetta approached the comet, the spacecraft became negatively charged, mostly due to photoelectrons of cometary origin, produced by photoionization of the outgassing neutral atmosphere of 67P. The cometary nature of these electrons can be identified by studying the correlation between the spacecraft potential and the projected latitude of Rosetta relative to the nucleus. Indeed, 67P is more active around the neck and in the Northern hemisphere than in the Southern hemisphere (when it is summer in the Northern hemisphere, as is the case for the data under consideration; e.g. Sierks et al. 2015; Fougere et al. 2016). The relationship between cometary neutral outgassing and spacecraft potential $V_{s/c}$ has been verified by Odelstad et al. (2015) in a comparison between RPC-LAP and the Rosetta Orbiter Spectrometer for Ion and Neutral Analysis (ROSINA). The latitudinal variations of the $V_{s/c}$ correspond to the 'envelopes' of the 6.2-h variations – half of the 12.4 spin period of the comet – related to the crossings of Rosetta above the very active comet neck region, as investigated in Edberg et al. (2015).

The illuminated spacecraft constantly produces photoelectrons, which form a photoelectron cloud around it when $V_{s/c}$ is positive. This means that, under those conditions, RPC-LAP measurements can be influenced by the photoelectron cloud. The photoelectron cloud is negligible for negative $V_{s/c}$ (Eriksson & Sjögren 2010). The effects of spacecraft-probe interactions are therefore not negligible, and this topic is studied in detail in Odelstad et al. (2016), where they also confirm that $V_{s/c}$ is proportional to the negative of the knee potential, i.e.

$$V_{s/c} \propto -V_k. \quad (2)$$

We denote the current in region 1 of Fig. 2 as I_1 in general, and evaluate I_1 at $V_k - 10$V and at $V_k - 20$V. The dominant contribution in sunlit conditions far away from the comet is the photoelectron emission current I_{ph}. Note that the sign of I_1 is defined, such that $I_1 \propto -I_{ph}$, in accordance with equation (A5). Closer to the comet, other contributions (ions, low-energy electrons and high-energy electrons) will start to play a significant role. When the plasma density increases, the spacecraft potential $V_{s/c}$ may flip from positive to negative. The density increase can also be seen in the increase of the region 3 electron current, denoted I_3. A varying $V_{s/c}$ with latitude can be related to an enhanced cometary outgassing resulting in enhanced plasma density (Odelstad et al. 2015). Following this, it is possible to regroup the observations between 2014 May and October into two main physical regions, (i) the solar wind

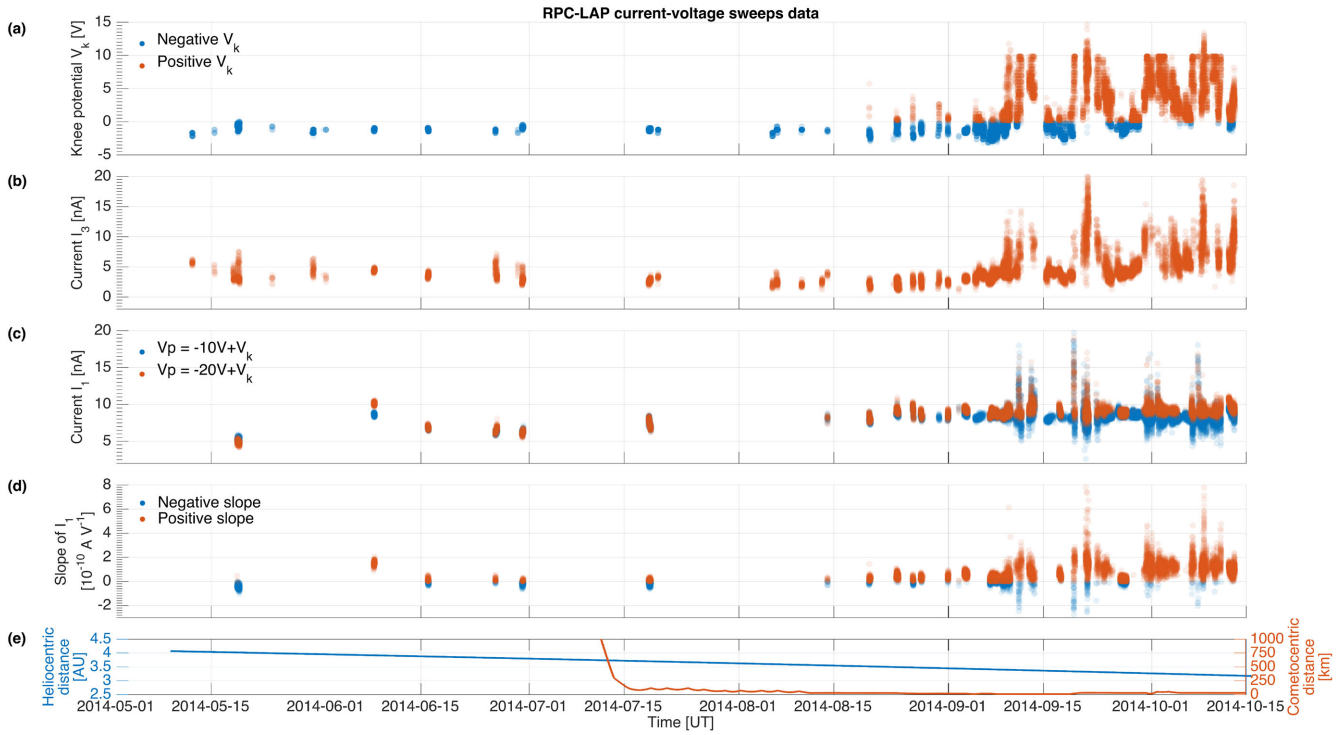

Figure 3. RPC-LAP1 measurements between 2014 May and October of (a) knee potential V_k, (b) I_3 current on the electron part (region 3) of the *I–V* characteristics, (c) I_1 current on the ion part of the *I–V* characteristics (region 1), evaluated at $-10\,\mathrm{V} + V_k$ in blue, and $-20\,\mathrm{V} + V_k$ in red, (d) the slope of I_1 between -10 and $-20\,\mathrm{V}$ from V_k, and (e) the heliocentric distance of Rosetta in au in blue (left axis) and its corresponding cometocentric distance in km in red (right axis). Large variations appear in the potential and the current from September onwards, although it is harder to discern a clear periodic oscillation in the I_1 data, suggesting the presence of multiple current contributions. The slope of I_1 is occasionally negative after September, which is a sign of secondary emission. In all four panels, the signals are initially seen to be dominated by photoelectron emission from EUV radiation. This is seen by the weakly negative V_k and the low I_1. These signals are drowned out by the larger cometary signals from September onwards.

dominated region prior to entry into 67P's plasma environment and (ii) the HDR dominated by 67P's plasma environment.

In order to study the evolution of the early cometary activity, based on the previous considerations, we focus on the temporal evolution of V_k, I_1 and I_3. The procedure for finding V_k, I_1 and I_3 is given in Appendix A. In short, V_k is first obtained by finding the peak of the second derivative of the smoothed *I–V* characteristics, traced by the solid blue curve in Fig. 2. Then, I_1 is evaluated at -20 and -10 V from V_k in the ion attraction part (red solid line in region 1 in Fig. 2), as well as the slope between the points. I_1 is divided into three measurements in order to clarify the different plasma contributions in this region. I_3, as a measure of the total electron current, is taken at a chosen bias in region 3. In Section 3, we present I_3 at the position $V_p = 7\,\mathrm{V}$, where V_p is the potential at the surface of the probe. The data range for this fit is the same for all sweeps, and is only dependent on the location of V_k. We chose the interval between -20 and -10 V because of voltage range limitations in one of our data blocks. Note that for our analysis, we are interested in relative variations of the measured currents, not the absolute values.

The impact of local ion density, secondary emission due to enhanced high-energy electron density, and interference from low energy on I_1, with respect to R_h, can then be explained in the following manner. When there is an increased ion density, the calculated I_1 will be larger (more negative in Fig. 2) than if it consisted only of the photoelectron emission current. However, we have not managed to separate this contribution from that of secondary emission arising from high-energy electrons in the ambient plasma. Secondary emission and unshielded low-energy electron current can together create what looks like an enhanced ion density, since their slopes can cancel each other, and create a flat line with a current I_1 which is more negative than for only photoelectron emission. A negative slope is a sign of secondary emission (e.g. see Garnier et al. 2013, who analysed Langmuir probe data from the Cassini spacecraft), while a positive slope is a sign of an increased density of low-energy electrons, and/or increased ion density. At the same time, I_1 evaluated at $V_k - 10\,\mathrm{V}$ can be more sensitive to the low-energy electron current bleeding into region 1, compared to I_1 evaluated at $V_k - 20\,\mathrm{V}$. The shape of their combined variations, compared with the slope, will allow us to discuss the presence of increased ion densities, secondary emission, and low-energy electron current. In the next section, we study the evolution of I_1, I_3 and V_k over time, solar distance, and cometary distance. Following Garnier et al. (2013), we define the high-energy electrons associated with secondary emission between 50–60 eV and 600–800 eV. When we discuss low-energy electrons, this means electrons which impinge directly on the probe in region 1 with an energy of the order of 20 eV, so that a certain amount of these electrons are filtered away when we compare measurements of I_1 at $V_k - 10\,\mathrm{V}$ against those at $V_k - 20\,\mathrm{V}$.

3 RESULTS

Fig. 3 displays RPC-LAP1-analysed data sets for the knee potential (panel a), current I_3 (panel b), current I_1 (panel c) evaluated at $-10\,\mathrm{V} + V_k$ in blue, and $-20\,\mathrm{V} + V_k$ in red, and the slope of I_1 (panel d), all between 2014 May and October. Panel (e) shows

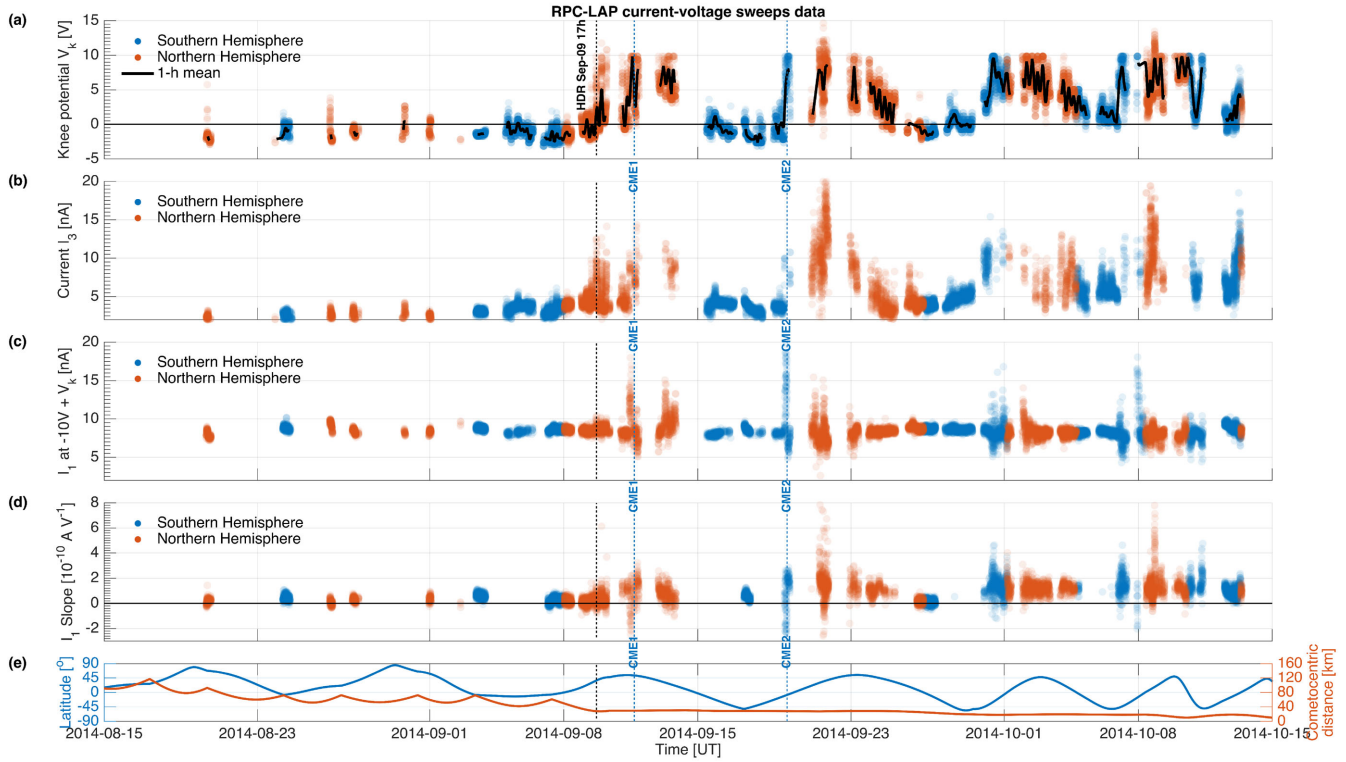

Figure 4. RPC-LAP1 measurements between 2014 August 20 and October 15 from sweeps of (a) knee potential V_k, (b) I_3 current on the electron attraction part (region 3) (c) I_1 current on the ion attraction part of the I–V characteristics (region 1) evaluated at $-10\,V + V_k$, (d) I_1 slope, sorted by 67P's Northern hemisphere in red and Southern hemisphere in blue. Panel (e) displays the latitude of Rosetta projected down on the nucleus in blue (left axis) and the cometocentric distance in km in red (right axis). The HDR was found at September 9, around 17:00 UT, and is marked in panel (a). This was determined by the first instance where the spacecraft had been negatively charged for more than 3 h. In all three panels, two CMEs, CME1 on 11-09 15:55 UT and CME2 on 19-09 19:00 UT, found by McKenna-Lawlor et al. (2016) are also shown. They correspond to V_k peaks, and to I_1 and I_3 current fluctuations. Note again that the current in panel (c) has the opposite sign as the one in the I–V characteristics.

the cometocentric distance in km and the heliocentric distance of Rosetta in au, as a function of time. We see that the heliocentric distance decreases linearly with time, while the cometocentric distance drastically decreases during the initial approach in mid-July. There is an additional dip as Rosetta entered the 30 km bound orbits in mid-September, as will be seen in Fig. 4.

As explained before, the knee potential measured by RPC-LAP1 and shown in Fig. 3(a) is proportional to the negative of the spacecraft potential $V_{s/c}$, and is also proportional to the negative of the logarithm of the density of local electrons charging the spacecraft when $V_{s/c}$ turns negative (Anderson et al. 1994). The spacecraft potential is initially slightly positively charged, before it starts to fluctuate towards negative charges in mid-August. These variations eventually develop into periodic oscillations. Within these oscillations are smaller, regular, oscillations with a period of 6.2 h. We therefore call the knee potential envelopes the larger oscillations containing the 6.2 h variations, which we briefly discussed in Section 2. Note that the sharp cutoffs of the envelope peaks above 10 V are due to insufficient sweep bias voltage range in one of the modes used in this part of the mission. Note also that the depth of the colour corresponds to the density of the points.

Fig. 3(b) shows I_3, the current measured in the electron attraction part of the I–V characteristics, evaluated at a fixed bias voltage, i.e. $V_p = 7$ V. This current is only due to electrons of all energies. The current to the probe increases with increasing local electron density. Thus, we see that the density of electrons varies as V_k shown in panel (a).

In Fig. 3(c), we see that both currents I_1 (at $V_k - 10$ and $V_k - 20$ V) start to oscillate following the onset of knee potential envelopes in early September. Generally speaking, I_1 is composed of the photoelectron emission current I_{ph}, as well as currents due to ions, secondary emission, low-energy electrons, and possibly direct (non-secondary emission) high-energy electrons. Far away from the comet, I_1 is expected to follow radiative solar flux dilution scaling in R_h^{-2} according to equation (1), and should therefore slant upwards as Rosetta approaches the Sun. An increasing ion population, as well as an increasing secondary emission, will push the I_1 current upwards, while an increasing low-energy electron contribution will push it downwards. The blue data points, measured at $V_k - 10$ V, fluctuate more downwards than the red points measured at $V_k - 20$ V. This means that the low-energy electron density is more pronounced in this current compared to the ion and secondary emission components. The small negative slope values found in the first half of panel (d) should be seen as an indication of the accuracy limit of the instrument. Its linear amplifiers inevitably result in some leakage current which is regularly measured onboard and corrected for onground (Eriksson et al. 2007), but some uncertainty remains. The higher negative values intermittently appearing in September and October are real and may possibly be due to secondary emission, though time variation of the plasma parameters during the sweep time is at least as likely.

Note that the difference in the data sampling between I_1 and I_3 is because the potential bias sweep is out of range, depending on the position of V_k. For high V_k (e.g. 10 V), I_1 is always in range but I_3

might not be. For low V_k (e.g. 0 V) the situation is reversed. Details on this can be found in the Appendix.

Since we see increased activity after mid-August, we show the zoomed-in part of the data between August 20 and October 15 in Fig. 4. In addition, we differentiate between the hemispheres of the comet in Fig. 4(a–d) with blue for the Southern hemisphere and red for the Northern hemisphere as colour code. We also show the projected latitudes of Rosetta relative to 67P in panel (e).

In Fig. 4(a), the black lines represent the 1-h means of V_k. We found that the best way to define the transition into the region of denser plasma connected to the knee potential envelopes was to consider the first instance where the spacecraft is negatively charged for a sufficiently long period of time. To decide on this threshold, the knee potential is first averaged over 1 h to remove random fluctuations (e.g. Pécseli 2000); then, to reach statistical significance, at least three consecutive intervals of 1-h negative potentials are needed for selection. The choice of a 3-h threshold is also connected to the longitudinal variation of the potential due to crossings of Rosetta above the more active neck region of the nucleus, i.e. about half of the 6.2-h variations that were noted earlier. By considering the first instance where the spacecraft was negatively charged for more than 3 h consecutively, we find the transition point to the HDR (for HDR) on September 9 around 17 UT. This corresponds to the onset of the first knee potential envelope. We note that the spacecraft is more negatively charged when in Northern latitudes, and less negatively charged, or even positively charged, in Southern latitudes, as observed by Odelstad et al. (2015). Moreover, using a 3D magnetohydrodynamics model to propagate the solar wind density and velocity, McKenna-Lawlor et al. (2016) recently found evidence in the RPC measurements of two CME events in 2014 September: CME1 on 11-09 15:55 UT and CME2 on 19-09 19:00 UT. On these occasions, the RPC-IES ion/electron spectrometer data witnessed sharp increases in energy flux in conjunction with increased magnetic fields and polarity changes from RPC-MAG. On average, according to the authors, each of these events may have affected the measurements up to several days after the initial onset. Following this study, we also marked the location of the two CMEs, both of which are close to peaks in V_k. Note that two of the clearest cases of secondary emission seem to correspond to the arrival of the CMEs.

In Fig. 4(b), I_3 fluctuates according to V_k, as expected, with clear hemispherical (latitudinal) dependence. Panel (c) shows that ions and/or secondary emission, seen by increases in the current, follow the same dependence, but low-energy electron density increases, seen as decreases in the current, are more irregular, and do not seem to be constrained to Northern hemispheres. Panel (d) shows that only a few of the certain secondary emission events (negative slope) correspond to positive current fluctuations in I_1, after removing the two secondary emission events corresponding to CMEs. This supports the interpretation of some of the remaining positive current fluctuations as ion density increases. Note also the two CME events are associated with large fluctuations of I_1, i.e. CMEs are associated with increases in both low-energy and high-energy electron densities. As can be inferred from Fig. 4(e), the first CME, CME1, corresponds to Rosetta's position at one of its northernmost latitudes. Consequently, the signals seen in RPC-LAP1 at the time of CME1 could also be simultaneously related to an increased plasma density.

Fig. 5 shows the current density corresponding to I_1 at (a) $V_k - 20$ V and at (b) $V_k - 10$ V from RPC-LAP1 in blue, and the integrated solar EUV flux in red, plotted against the heliocentric distance R_h. The current density in nA m^{-2} is simply obtained by dividing the I_1 current by the sunlit area of the probe, i.e. πr^2 with $r = 0.025$ m. The solar EUV flux is obtained by propagating measurements by TIMED/SEE at Earth (at 1 au; e.g. Woods et al. 2005) out to Rosetta's position at 67P. The propagated EUV flux at a certain Rosetta epoch is based on the TIMED/SEE differential fluxes at the last preceding or first succeeding epochs when Earth's solar longitude was the same as Rosetta's at the queried epoch, whichever gives the least time shift. If the Earth-Rosetta time shift is more than ± 7 d, a weighted average of the preceding and succeeding TIMED/SEE measurements at the current Rosetta solar longitude is used. This is then multiplied by a R_h^{-2} scaling factor with respect to the heliocentric distance and integrated for wavelengths below 150 nm to account for the bulk of the photoionization.

The two regions of study mentioned previously in Section 2, i.e. (i) solar wind dominated convection electric field region and (ii) HDR, can be clearly seen when looking at the variations of the current density. We take a least-squares power-law fit through the data on both sides of the HDR, identified previously on 09-09 around 17 UT with the knee potential. If the escaping photoelectrons from the probe dominate the measurements, the fit will be close to R_h^{-2}, as expected from equation (1). The fit on the right-hand side, in region (i), is the solid black line, and scales as (a) $R_h^{-2.03}$ and (b) $R_h^{-1.96}$, which are both close to the theoretical expectations. On the other hand, the fit through the entire measurement set goes as (a) $R_h^{-1.54}$ and (b) $R_h^{-0.83}$. This shows that there is a transition between photoelectron measurements and the non-negligible appearance of other current contributions near the HDR region, produced by the higher density of plasma within the HDR. Also, the power-law fit through the region after the transition changes sign and is negatively sloped in (b), as opposed to in (a), which suggests that from the point of view of RPC-LAP, the HDR can be defined more by a density increase of low-energy electrons than that of ions and secondary electrons. Furthermore, since both CME1 and CME2 occur after the HDR, the transition should not be a result of a CME impact, although they possibly affect the measured currents after September 11 when the first CME hits the comet.

Note that since the I_1 current density is an indicator of mainly photoelectron emission prior to entry into the HDR, our pre-HDR fit can be extrapolated to $R_h = 1$ au distance and compared to previous photoelectron emission measurements near Earth. We find for $I_1(V_k - 20)$ a current density of 52.9 μA m^{-2}, and for $I_1(V_k - 10)$ a current density of 48.8 μA m^{-2}. Pedersen (1995) found photoelectron current densities between 40 and 80 μA m^{-2} at 1 au on the basis of satellites GEOS-1, GEOS-2, ISEE-1, Viking, and CRRES; it depends on the coating material of the probes and the solar EUV flux. This range can be narrowed down using the photoemission current–spacecraft voltage relations in Scudder et al. (2000). We can estimate the early (positive) spacecraft potential as no lower than 2 eV using a conversion factor of 1.5–2 between V_k and $V_{s/c}$ (as in Edberg et al. 2015). Fig. 2 in Scudder et al. (2000) then predicts for different materials a photoemission current in our pre-HDR conditions no higher than 50–60 μA m^{-2}, which is in very good agreement with our results.

4 DISCUSSION

In Section 3, we found a transition into the HDR on September 9, at a cometocentric distance of 28 km, and a heliocentric distance of 3.395 au, as seen by V_k and validated by our study of the I_1 current. After entry into the HDR, the oscillations of I_1 and I_3 suggested a cometary source for the increased plasma density.

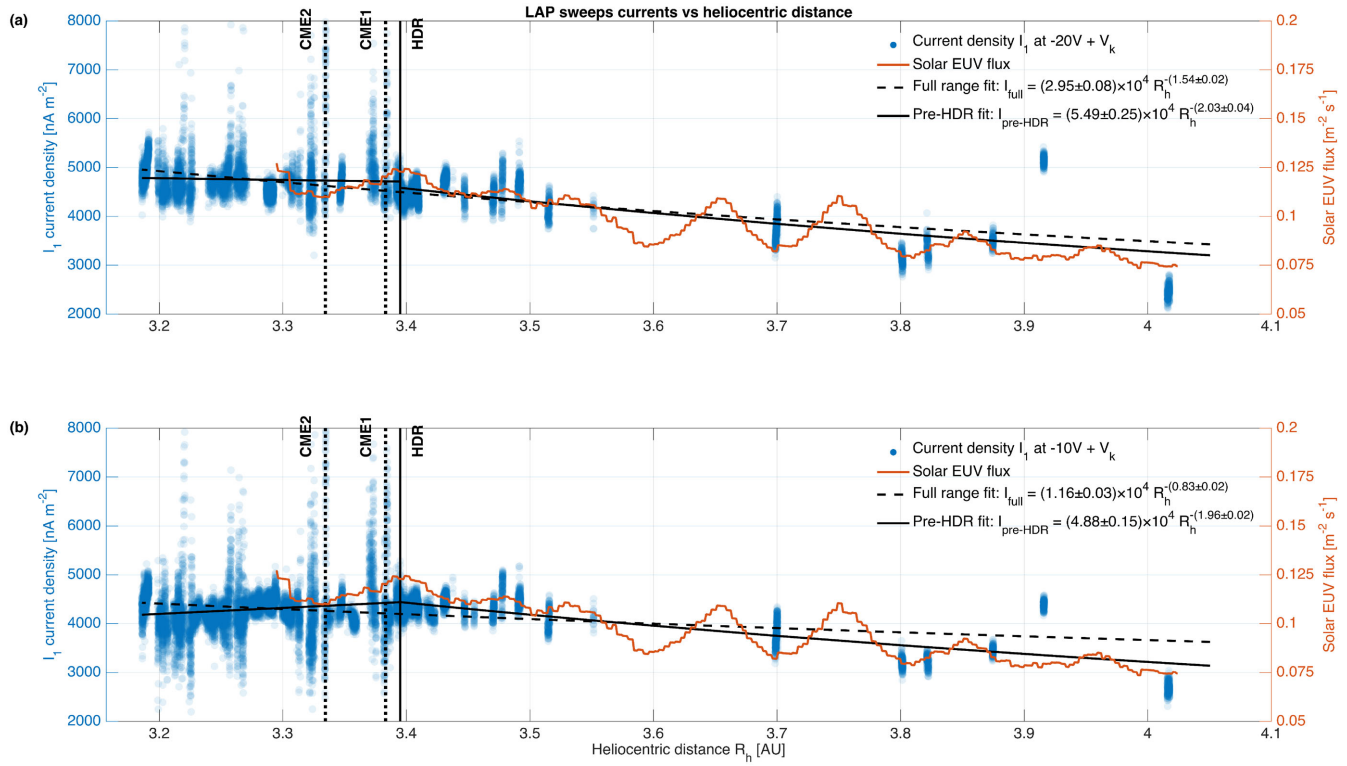

Figure 5. (a) Current density for I_1 evaluated at $V_k - 20$ V and (b) current density for I_1 evaluated at $V_k - 10$ V. Both are in units of nA m^{-2} in blue (left axis), and plotted against heliocentric distance in au and integrated, propagated and scaled (to R_h) solar EUV flux with its typical 27-d oscillations in red (right axis). A least-squares power-law fit is performed on either side of the high-density region (marked HDR by a vertical solid line, September 9 around 17:00 UT) and also through the entire measurement set. The pre-HDR (solar wind region) fit goes as $R_h^{-2.03}$ in (a) and $R_h^{-1.96}$ in (b), while the fit through the entire measurement set goes as $R_h^{-1.54}$ in (a) and $R_h^{-0.83}$ in (b). Note that the fit in the HDR evaluated at $V_k - 20$ V in panel (a) has a larger slope than in panel (b), which shows that, for the HDR seen as a whole, the low-energy electron contributions dominate over secondary emissions. CME1 and CME2 from McKenna-Lawlor et al. (2016) are shown as dashed lines.

Since the definition of the HDR is a conservative estimate (first instance of consecutive 3 h of negative spacecraft potential during the approach trajectory towards 30 km orbits), the first appearance of the high plasma densities may occur at a slightly larger cometocentric distance. Consequently, we now study the spatio-temporal evolution of the transition with respect to cometocentric distance.

V_k, I_3 and I_1 at $V_k - 10$ V, versus cometocentric distance, are presented in Fig. 6, colour-coded with respect to time. To remove the contribution of CME impacts found by McKenna-Lawlor et al. (2016) on September 11 and 19, RPC-LAP1 current and knee potential data points have been removed up to one day before and after each event. As the spacecraft approaches the 30 km bound orbits, V_k significantly increases from -2 V to more than 5 V on average. From Fig. 4 in Section 3, we see that this increase happens before the first CME event. We associate this behaviour with increased local plasma density. Highly negative spacecraft charge also occurs later on, for instance, near October 1, at approximately the same cometocentric distance. It is therefore also possible that the region of enhanced plasma density is present in the Northern hemisphere, as well as in certain areas of the Southern hemisphere, in accordance to activity levels. In Fig. 6, V_k sharply increases following entry into 30 km orbits, and is only lower between 20 and 30 km because Rosetta is in Southern latitudes in this period. When Rosetta moves from 10 to 30 km after October 15 during Northern latitudes (not shown), V_k reaches larger values. In Fig. 6 (b), we also notice that the increase in electron density occurs between 30 and 27 km, before our placement of the HDR. The same is true in panel (c), for both movements below the average I_1 (associated with increased density of low-energy electrons) and movements above the average I_1 (associated with secondary emission and higher ion densities) seen on the upper parts of the data (above ∼7 nA), also between 30 and 27 km. This suggests that the HDR may occur between 27 and 30 km from the comet.

The HDR may grow as 67P gets closer to the Sun, and this could be studied over longer heliocentric distances than presented here. The possible movement of the HDR boundary into larger cometocentric distances as a result of increased cometary activity (characterized by increased neutral outgassing) is especially interesting, since we see that Rosetta exits the HDR for Southern hemispheres, as during the trajectory between 27 and 18 km in these panels. Later crossings of the same distance for the Northern hemisphere (not shown) show increased V_k. This suggests that the HDR exists within a radius from the nucleus of the comet, but is latitudinally constrained during at least the early part of the mission.

In the following paragraphs, we interpret the sudden increase of plasma density by linking it to several possible causes for transition into the HDR, all related to comet–Sun interactions. The existing literature on 67P furnishes several possibilities. Related physical characteristics in the early activity of 67P are the pick-up ions observed by IES and ICA in August and September, mentioned in Section 1, sudden increases in the solar wind density and velocity, such as those associated with CMEs, seasonal variations in the outgassing from the cometary nucleus, and RPC-MAG's observation

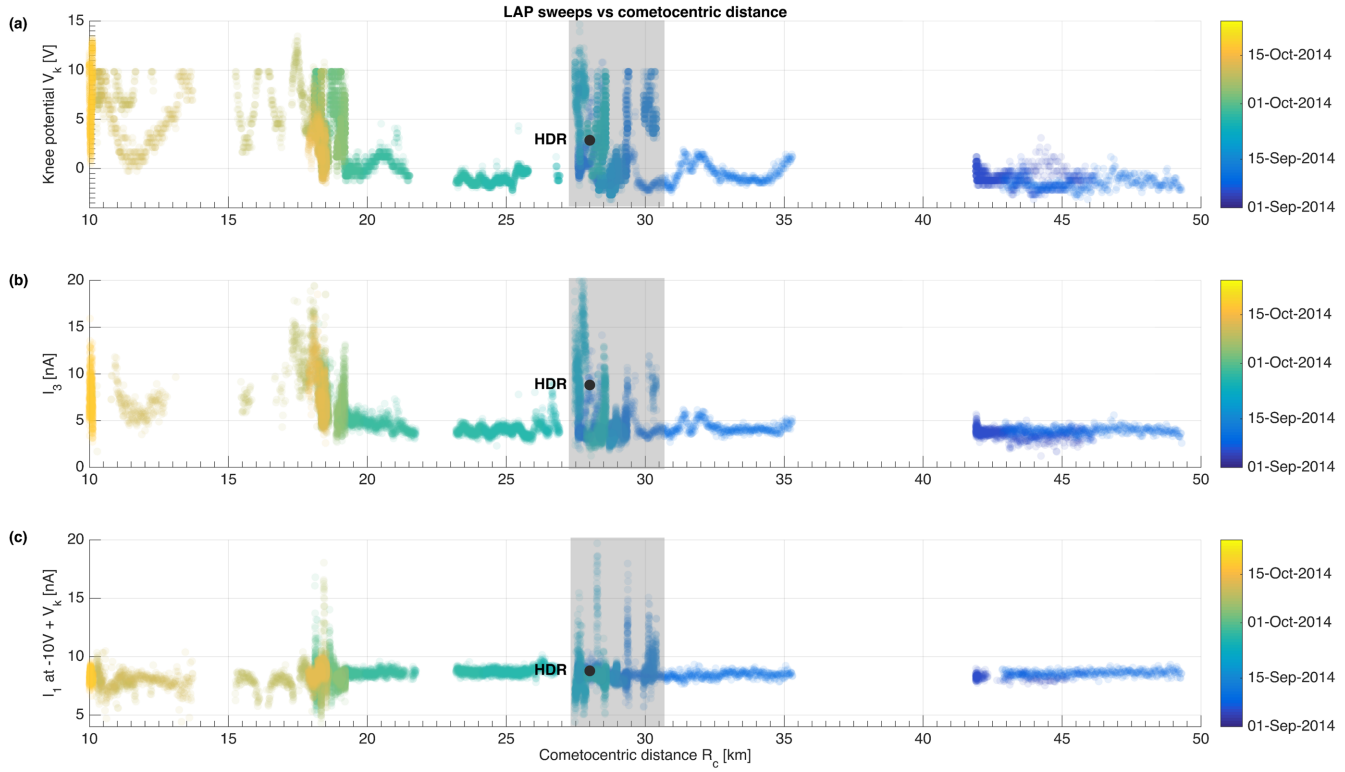

Figure 6. RPC-LAP1 measurements of (a) V_k, (b) I_3, and (c) I_1 at $V_k - 10$ V, from 2014 September through October, plotted against cometocentric distance R_c in km. In both panels, the timeline of the measurements is shown in the colour bar. We mark the positions of the high-density region (HDR) at 28 km from the nucleus. Note the slope on the lower side of I_1 between 30 and 27 km. We ascribe this to an increase of high-energy electrons from 30 km onwards. The variations of V_k and I_1 associated with the CMEs have been removed, up to 1 d after each event, following McKenna-Lawlor et al. (2016). Note that the quiet region between approximately 18 and 27 km is due to Rosetta sampling the Southern hemisphere. Evidently, HDR is localized in Northern hemispheres during the early phase of the mission. The shaded area corresponds to the approximate extent of the HDR before Rosetta exits the Northern hemisphere.

of a low-frequency wave flattening near the entry into the 30 km bound orbit. We also investigate whether the oscillation in our signals is related to the natural oscillation of the solar EUV flux, and the connection between our signals and the seasonal variations typical of water-group ions and their associated electrons.

We first consider whether the observations are related to pick-up ions. RPC-IES published observations of pick-up ions for the early plasma environment of 67P, manifested as high-energy spikes in their ion spectograms (Goldstein et al. 2015). Subsequently, IES picked up energetic negatively charged particles (Burch et al. 2015) in the solar wind in the span of 2014 mid-September to mid-December, a time period whose start coincides with the 30 km orbits following transition into the HDR. These spectra were different, and the earliest date for pick-up ions was August 7, i.e. over a month before entry into the HDR. The region characterized by pick-up ions therefore sits outside of, and possibly encompasses parts of, the HDR.

We also consider transient enhancement of the solar wind, such as CMEs. McKenna-Lawlor et al. (2016) traced CMEs from satellite measurements until impact at 67P during 2014 September. The three ejections travelled from the Sun on September 1, 9, and 10, and took 10 d to arrive at 67P, but only two of them had a clear impact. RPC-LAP senses a large increase of plasma during each CME passage on September 11 and 19, with elevated plasma density after. We can differentiate the spiky CME signatures in Fig. 4 from the oscillations in September which correspond to seasonal effects. The spikes also do not manifest until approach into the 30 km orbits. By factoring in the CMEs studied by McKenna-Lawlor et al. (2016), we can remove two of the large spikes in the September data so they do not appear in Fig. 6.

Another possibility relates to excessive variations of the solar EUV radiation, since the current intensities collected by RPC-LAP sweeps depend on the illumination and ultimately on the solar EUV flux. Thus, a variation in EUV flux should be seen as a variation in the collected photoelectron current density by the probe and qualitatively follow each other. Until the end of 2014 August, the solar EUV flux variations match those of the RPC-LAP current measurements, with a slow increase of the photoelectron emission that can be linked directly to the increase in the flux, as the heliocentric distance between Rosetta and the Sun decreases. The 27-d periodicity in the EUV flux, due to the Sun's rotation (e.g. Woods & Rottman 2002), has an impact on the photoelectron emission yield of the probes, resulting in the EUV flux and the I_1 current density being in qualitative agreement. After the end of 2014 August, this trend starts to be significantly altered, with the I_1 current density exhibiting large variations that do not correlate any more with the solar EUV flux variation. At the time of the transition into the HDR, the solar EUV flux variations stop driving the evolution of the I_1 currents. Thus, some other effects begin to take precedence on 2014 September 9, and the transition found in the RPC-LAP photocurrent measurements is probably not a temporally isolated artefact due to a sudden variation of the solar flux.

On the temporal scale that we study in this paper, we see oscillations of the knee potential, as well as traces of this in the ion attraction current I_1. These signals correspond to the envelopes of the 6.2-h longitudinal oscillations reported by Odelstad et al. (2015)

and Edberg et al. (2015), and relate to repeated crossings of more active regions on the comet (with increased neutral outgassing). The envelopes correspond to latitudinal variations, where the Northern hemisphere of 67P is the more active one, and can be seen for electrons with RPC-IES as early as in August (Clark et al. 2015), but at a smaller energy and density compared to 2014 September. Although part of the reason for the spread seen at 27–29 km from the nucleus is the oversampling of the projections of active regions once Rosetta enters into the 30 km orbit, this does not explain the sudden change of magnitude upon approach to this orbit. Rosina's Double Focusing Mass Spectrometer (DFMS) measurements show increased density of O_2 following entry into the 30 km orbit in September (Bieler et al. 2015), which Bieler et al. (2015) showed had a correlation coefficient with H_2O of 0.88 in general, and 0.97 for 2014 October. The density also varies according to the diurnal cycle of water ice on the surface of the comet (De Sanctis et al. 2015). Thus, the long-period oscillations (envelopes) seen in $V_{s/c}$ and I_3 are likely due to variations of the associated electrons arising from freshly ionized water-group ions. In Fig. 6, we also find that the cometary plasma activity increases discontinuously near the entrance to the 30 km orbits. This strengthens the argument that the transition into the HDR corresponds to observations of increased plasma density of cometary origin. Furthermore, Edberg et al. (2015) show a relation for an estimated density of ions in 2015 February which corresponds to the neutral outgassing model of Haser (1957) applied to the production rate of an ionized coma with the nucleus as source. However, the Haser model is a spherically symmetric model of the neutral coma expansion, whereas 67P is not spherically symmetric. Thus, the fact that outgassing rate is a function of latitude accounts for the seasonal dependence of the HDR, and suggests that the entrance into the HDR can change with both the latitude and the activity of the comet.

Finally, RPC-MAG results also support the interpretation of the sudden increase of plasma ions in independent measurements during the same transition to the 30 km orbit. Richter et al. (2015) found a continuous growth of the magnetic energy density of waves in the range between 30 and 80 mHz from 100 to 30 km distance from the nucleus. This growth saturated near 30 km, with a large variation of energy density at this distance, and again near 20 km, both of which can be attributed to increased sampling of different regions once Rosetta entered into the bound orbits in September. These results are analogous to the density enhancement signatures which were presented in Fig. 6. Richter et al. (2015) suggested that the wave flattening is due to a cross-field current perturbation, which we would see with RPC-LAP as the transition into the HDR. Numerical simulations by Koenders et al. (2013) and Koenders et al. (this issue) explore this question in more detail. Our results from RPC-LAP presented in this paper independently support their argument that the wave flattening is associated with a sudden plasma density increase.

In order to further understand this phenomenon, future work should study whether the position of the HDR evolves as 67P becomes more highly active. Several ways can be used to separate the early against the highly active plasma environment of 67P. Observations with ROSINA, RPC-ICA and RPC-IES from late October through mid-December show the continuous presence of the solar wind during the 30 km orbits, and that the solar wind has direct access to the nucleus in this time period (e.g. Fuselier et al. 2015; Nilsson et al. 2015b). The results from this paper need therefore to be compared to the active coma by looking for the HDR in an environment where the nucleus is shielded from the solar wind. It is also known that for rarefied plasma, binary collisions are rare, and damping of magnetohydrodynamic waves in the solar wind is driven by Landau damping due to Cherenkov resonance with cometary ions (Galeev & Sagdeev 1988). As the coma becomes more active, collisions increase, and we can therefore study the HDR observed at different solar distances in the context of non-collisional and collisional wave signatures.

Hybrid simulations in Rubin et al. (2014) suggested that Rosetta would not find a bow shock or early plasma transition during the approach phase. The transition into a high-activity coma should be manifested by the appearance of transition regions such as the bow shock, cometary ionosphere, and diamagnetic cavity (Cravens & Gombosi 2004; Koenders et al. 2013). We will thus investigate whether the HDR transitions could be related to the boundary signatures known from simulations and previous fly-bys of comets. One example of such an approach are the measurements of strong fluxes of accelerated water ions by RPC-ICA (Nilsson et al. 2015b) during the 250 km excursion in 2015 February, compared to the weaker signals from the same distance in 2014 August. Note that the 2014 to 2015 activity of 67P differed slightly from that of the passage in 2008 (e.g. Hansen et al. 2016; Simon Wedlund et al. 2016), which introduces yet another complexity to the analysis.

Up to at least a heliocentric distance of 2.8 au, the ion dynamics around the nucleus is driven by solar wind mass-loading effects, as it is observed by particle and magnetic field instruments (Coates et al. 2015; Nilsson et al. 2015a; Behar et al. 2016). Behar et al. (2016) recently hypothesized that both solar wind convection electric field and an antisunward polarization electric fields acting on accelerated cometary ions are needed to capture the complexity of the observations in terms of slowing down of the flow and angular dispersion. Such effects have yet to be explored in simulations. Our finding in this paper of a sharp transition between a solar wind convection electric field region and a region of increased local plasma density is therefore a step towards understanding the low-activity coma, characterized by an absence of clear plasma boundaries.

5 CONCLUSION

Using RPC-LAP onboard Rosetta, we found that comet 67P's early plasma atmosphere at a heliocentric distance of 3.4 au was composed of two regions. There is an outer region mostly dominated by the solar wind's convection electric field, where pick-up ions are shown to exist by other RPC instruments onboard Rosetta. In this region, the spacecraft is positively charged by photoelectron emission due to solar radiation, and RPC-LAP1, when sunlit and negatively biased, collects primarily a photoelectron emission current, with a characteristic scaling in $1/R_h^2$, with R_h the heliocentric distance of the spacecraft. At approximately 30 km from the nucleus for Northern latitudes, Rosetta enters a high-plasma density region, which we name HDR. Inside the HDR, the increased plasma density manifests in the collected current I_1 in the ion attraction region of the I–V characteristics as a combination between ion current, low-energy electron contamination, and secondary emission associated with high-energy electrons. $V_{s/c}$ then turns negative and the amplitude of its fluctuation, following the north–south latitudinal neutral asymmetry, increases. I_3, which is a proxy of the total electron density, and I_1, which represents a combination of variations in density for ions and low- and high- (from secondary emission) energy electrons, both follow $V_{s/c}$ and the north–south latitudinal variations. Simulations by Koenders et al. (2013) and Koenders et al. (this issue) have predicted the appearance of this inner region of enhanced plasma density. Another new observation is the appearance of secondary emission due to high-energy electrons concurrent

with increased ion density, both of which follow $V_{s/c}$ and latitudinal variations, and therefore likely correspond to cometary water-group ions and their associated electrons. One interesting point is that the HDR seems to form only in the Northern hemisphere throughout 2014 September to November. We also showed that photoelectron emission variations in I_1 are drowned out by the signals of local plasma once Rosetta enters the HDR.

ACKNOWLEDGEMENTS

The authors wish to thank Arne Pedersen and Hans Pécseli for helpful discussions, and Bjørn Lybekk for data management and access, as well as all students in the Rosetta UiO literature review team, many of whom transitioned into Rosetta-themed thesis work. We also wish to thank the creators and maintenance workers of the SPICE toolkit and the ESA Rosetta kernels for accurate mapping of the relative distances of our data to the Sun and 67P. This research is supported by the Research Council of Norway grant no. 240000. This work is also a part of the 4DSpace Strategic Research Initiative at the University of Oslo. The work on RPC-LAP in Uppsala was funded by the Swedish National Space Board under contracts 109/12 and 135/13, and by Vetenskapsrådet under contract 621-2013-4191. The authors wish to acknowledge also the AMDA science analysis system provided by the Centre de Données de la Physique des Plasmas (CDPP) supported by CNRS, CNES, Observatoire de Paris and Université Paul Sabatier, Toulouse. Rosetta is an ESA mission with contributions from its member states and NASA.

REFERENCES

Allen J. E., 1992, Phys. Scr, 45, 497
Anderson P. C., Hanson W. B., Coley W. R., Hoegy W. R., 1994, J. Geophys. Res.: Space Phys., 99, 3985
Behar E., Nilsson H., Wieser G. S., Nemeth Z., Broiles T., Richter I., 2016, Geophys. Res. Lett., 43, 1411
Bieler A. et al., 2015, Nature, 526, 678
Brace L. H., 1998, in Borovsky J., Pfaff R., Young D., eds, Measurement Techniques in Space Plasmas: Particles (AGU Geophysical Monograph 102). American Geophysical Union, Wasington DC, p. 23
Brace L. H., Hoegy W. R., Theis R. F., 1988, J. Geophys. Res.: Space Phys., 93, 7282
Burch J. L., Cravens T. E., Llera K., Goldstein R., Mokashi P., Tzou C.-Y., Broiles T., 2015, Geophys. Res. Lett., 42, 5125
Carr C. et al., 2007, Space Sci. Rev., 128, 629
Clark G. et al., 2015, A&A, 583, A24
Coates A. J., 1997, Adv. Space Res., 20, 255
Coates A. J., Jones G. H., 2009, Planet. Space Sci., 57, 1175
Coates A. J., Burch J. L., Goldstein R., Nilsson H., Stenberg Wieser G., Behar E., the RPC Team, 2015, J. Phys. Conf. Ser., 642, 012005
Combi M. R., Feldman P. D., 1993, Icarus, 105, 557
Cravens T. E., Gombosi T. I., 2004, Adv. Space Res., 33, 1968
De Sanctis M. C. et al., 2015, Nature, 525, 500
Edberg N. J. T. et al., 2015, Geophys. Res. Lett., 42, 4263
Edberg N. J. T. et al., 2016, J. Geophys. Res., 121, 949
Eriksson A. I., Hänberg C., Sjögren A., 2010, Proc. 11th Spacecraft Charging Technology Conference (SCTC-11), Albuquerque, NASA. Available at http://www.space.irfu.se/aie/Eriksson2010a.pdf
Eriksson A. I., Winkler E., 2007, Proceedings of the 10th Spacecraft Charging Technology Conference
Eriksson A. I. et al., 2007, Space Sci. Rev., 128, 729
Fougere N. et al., 2016, A&A, 588, A134
Fuselier S. A. et al., 2015, A&A, 583, A2
Galeev A. A., Sagdeev R. Z., 1988, Ap&SS, 144, 427
Garnier P. et al., 2013, J. Geophys. Res.: Space Phys., 118, 7054
Glassmeier K.-H., Boehnhardt H., Koschny D., Kührt E., Richter I., 2007a, Space Sci. Rev., 128, 1
Glassmeier K.-H. et al., 2007b, Space Sci. Rev., 128, 649
Goldstein R. et al., 2015, Geophys. Res. Lett., 42, 3093
Grard R. J. L., 1973, J. Geophys. Res., 78, 2885
Hansen K. C. et al., 2007, Space Sci. Rev., 128, 133
Hansen K. C. et al., 2016, MNRAS, in press
Haser L., 1957, Bull. Soc. R. Sci. Liege, 43, 740
Huebner W., Mukherjee J., 2015, Planet. Space Sci., 106, 11
Koenders C., Glassmeier K.-H., Richter I., Motschmann U., Rubin M., 2013, Planet. Space Sci., 87, 85
McKenna-Lawlor S. et al., 2016, Earth Moon Planets, 117, 1
Magnus F., Gudmundsson J. T., 2008, Rev. Sci. Instrum., 79, 073503
Medicus G., 1961, J. Appl. Phys., 32, 2512
Medicus G., 1962, J. Appl. Phys., 33, 3094
Nilsson H. et al., 2007, Space Sci. Rev., 128, 671
Nilsson H. et al., 2015a, Science, 347, aaa0571
Nilsson H. et al., 2015b, A&A, 583, A20
Odelstad E. et al., 2015, Geophys. Res. Lett., 42, 10126
Odelstad E., Stenberg-Wieser G., Wieser M., Eriksson A. I., Nilsson H. L. J. F., 2016, Proc. '14th Spacecraft Charging Technology Conference'. European Space Agency, Noordwijk, p. 123
Pécseli H. L., 2000, Fluctuations in Physical Systems. Cambridge Univ. Press, Cambridge
Pedersen A., 1995, Ann. Geophys., 13, 118
Richter I. et al., 2015, Ann. Geophys., 33, 1031
Rubin M. et al., 2014, Icarus, 242, 38
Schott L., 1968, in Lochte-Holtgreven W., ed., Electric Probes. North-Holland Publishing Company, Amsterdam, p. 668
Scudder J. D., Cao X., Mozer F. S., 2000, J. Geophys. Res., 105, 21
Sierks H. et al., 2015, Science, 347, aaa1044
Simon Wedlund C. et al., 2016, A&A, 587, A154
Snodgrass C., Tubiana C., Bramich D. M., Meech K., Boehnhardt H., Barrera L., 2013, A&A, 557, A33
Trotignon J. G. et al., 2007, Space Sci. Rev., 128, 713
Woods T. N., Rottman G. J., 2002, in Mendillo M., Nagy A., Waite J. H., eds, Atmospheres in the Solar System: Comparative Aeronomy. American Geophysical Union, Washington DC, p. 221
Woods T. N. et al., 2005, J. Geophys. Res., 110, A01312

APPENDIX A: ANALYSIS OF RPC-LAP DATA

The spherical Langmuir probe instrument on Rosetta, RPC-LAP (Eriksson et al. 2007; Eriksson et al. 2008), has a set of operational modes, most of them including the probe bias voltage sweeps we use in this study. In the time period considered in this article, we use data from three different sweep modes. Their potential bias range is [−30, 30], [−30, 20], and [−12, 12] V. The sweeping voltage bias range puts limits on the energies of the plasma that can be probed. Since these modes do not overlap in time, it is important to define a consistent way to analyse them.

As the probe sweeps its potential, an electric current will be collected to its surface. When the potential at the surface of the probe is positive with respect to the local plasma potential, electrons are accelerated towards the probe and some ions are scattered away. This situation is reversed when the probe potential is negative. From the resulting current–voltage *I*–*V* characteristics, one can, in theory, derive moments of the plasma, i.e. density and average energy (temperature). In the following analysis, we follow the convention that collected electrons are measured as a positive current, and the ions as a negative current.

To determine the plasma potential near the probe surface, we use the fact that the second derivative of the *I*–*V* characteristics has its maximum when the probe bias is neutral to the locally surrounding plasma (Schott 1968; Brace 1998). This approach has

limitations since the measured *I–V* characteristics is noisy, and the second derivative of the noise may be higher than the peak of the second derivative. To circumvent this problem in the analysis, the *I–V* characteristics are smoothed with a moving Blackman window filter (Magnus & Gudmundsson 2008).

The RPC-LAP surface potential is heavily influenced by the potential of the spacecraft (Odelstad et al. 2016). In the solar wind and far from the comet, the spacecraft potential $V_{s/c}$ is controlled by the photoelectron emission current, being positive, while closer to the comet, it becomes usually negative (Odelstad et al. 2015). This will divide the measurements in two regions, when the electrons are accelerated towards the probe in the sheath of the spacecraft (for $V_{s/c} > 0$), and when they are decelerated ($V_{s/c} < 0$). When $V_{s/c} < 0$, the electrons will lose energy, until they are either absorbed by the probe or spacecraft, or scattered away. The amount of energy the electrons will lose or gain while reaching the probe is eV_k, since $-V_k$ is proportional to $V_{s/c}$ at the distance of the probe (Odelstad et al. 2016).

A1 Theory

In the following analysis, we follow the orbit motion-limited (OML) theory for the probe charging (Schott 1968). This is justified by the thick sheath around the probes and spacecraft. During early activity, Rosetta travels between the approximate distances of 3–4 au from the Sun. The density of plasma in the solar wind at 1 au is of the order of $n \sim 10^6 \mathrm{m}^{-3}$, which corresponds to a Debye length of $\lambda_{D,\,1\,\mathrm{au}} = 10$ m. Since the number density of the spherically expanding solar wind decreases with the distance to the Sun, R_h, as $n \propto R_h^{-2}$, the Debye length-scales as $\lambda_D \sim R_h$, and the Debye shielding at $R_h \sim$ 3–4 au is of the order of $\lambda_D \sim 30$ m. The distance between the spacecraft and the probe is 2.24 m for LAP1, and 1.62 m for LAP2, while the probes themselves have radii of 2.5 cm (Eriksson et al. 2007). The probes are then within the sheath of the spacecraft by a good margin, and $V_{s/c}$ is expected to affect the measurements. The OML limit is expected to be valid when the spacecraft enters the bound orbits close to the comet. There are three important components to the total current received by the probe; ion, electron, and photoemission current. The ion and electron currents are orbital motion-limited (Schott 1968). The collected electron current, I_e, as a function of the potential at the probe surface, V_p, is given by

$$I_e = \begin{cases} I_{0e}\left(1 + \frac{eV_p}{kT_e}\right), & V_p > 0 \\ I_{0e} e^{\frac{eV_p}{kT_e}}, & V_p < 0, \end{cases} \quad \text{(A1)}$$

where I_{0e} is the thermal current that would be received by a spherical probe neutral to the surrounding plasma, given a Maxwellian velocity distribution for the electrons of temperature T_e.

In a first approximation, ions are considered cold and the flow is supersonic. As such, the ions will not follow the same equation as for the electrons when repelled by the probe, see e.g. Allen (1992). However, the equation is similar to that of the electrons when they are attracted by the probe (Medicus 1961, 1962). For $V_p < 0$,

$$I_i = -I_{0i}\left(1 - \frac{eV_p}{E_i}\right), \quad \text{(A2)}$$

where the energy of the ions is $E_i = mv^2/2$. I_{0i} is the ion current that would be received by a spherical probe neutral to the surrounding plasma, i.e. at the local plasma potential. As for the retarded ion current (corresponding to the region of attractive electron potential), A2 is valid up to $V_p = mv^2/2e$ and $I_i = 0$ for higher V_p.

The photoelectron emission current is given by (Grard 1973),

$$I_{ph} = \begin{cases} -I_{0ph}, & V_p < 0 \\ -I_{0ph}\left(1 - \frac{eV_p}{kT_{ph}}\right) e^{-\frac{eV_p}{kT_{ph}}}, & V_p > 0, \end{cases} \quad \text{(A3)}$$

where I_{0ph} is the photoelectron emission current produced by the illuminated area of the probe, and T_{ph} is the temperature of emitted electrons. It is assumed that the photoelectrons leave the probe radially and that their velocity distribution is Mawellian. I_{0ph} depends on the material of the probe (TiN for RPC-LAP), the EUV-flux, and the area illuminated.

A2 *I–V* curve analysis techniques

With respect to infinity, the potential at the surface of the probe V_p is

$$V_p = V_s + V_b = V_b - V_k, \quad \text{(A4)}$$

where V_s is the plasma potential. V_b and V_k are the bias and knee potentials, respectively (see also Fig. 2). The knee potential, V_k, is the first parameter that needs to be obtained in order to determine V_p. This is done by taking the second derivative of the *I–V* sweep data. Since the plasma is very tenuous in the solar wind, the knee is not sharp enough to be detected in a reliable and automatic way if the probe is not sunlit. It is therefore required that the probe is sunlit, which creates a much sharper knee in the *I–V* curve due to photoelectron emission. With a typical noise level of ± 1 nA (as epitomized in Fig. 2), the data need to be smoothed in order to reduce the noise so that a peak in the second derivative of the corresponding *I–V* characteristics can be found. Due to the different voltage resolutions of the potential bias sweeping modes, V_k will have the same accuracy as the resolution of the mode from which it is derived. Two of the modes have a resolution of $\Delta V = 0.25$ V, and the other $\Delta V = 0.5$ V.

To possibly investigate ion parameters, we wish to analyse a part of the *I–V* curve that has as small a contribution from cold electrons as possible. Assuming only ion, photoelectron emission, and cold electron contributions, the total current for $V_p = V_b - V_k < 0$ is

$$I = -I_{0ph} - I_{0i}\left(1 - \frac{eV_p}{E_i}\right) + I_{0e} e^{\frac{eV_p}{kT_e}}, \quad \text{(A5)}$$

from equations (A1)–(A4). We then need $V_b - V_k$ to be negative enough so that

$$I_{0e} e^{\frac{eV_p}{kT_e}} \approx 0, \quad \text{(A6)}$$

and equation (A5) will then reduce to a linear form,

$$I = a + bV_p, \quad \text{(A7)}$$

where $a = -I_{0ph} - I_{0i}$, and $b = I_{0i}e/E_i$. The intercept a will then contain information on the ion density and temperature, as well as photoelectron emission current. However, contribution from hot electrons should still be present in both the intercept and the slope in (A7). There is also the possibility of contributions due to secondary emission as discussed in Garnier et al. (2013) for the Langmuir probe onboard Cassini. The photoelectron emission current is quite stable, following EUV flux variations. The dynamic nature of the atmosphere of comet 67P would thus reveal itself as fluctuations in the current described by (A7), and would mostly be due to variations in the surrounding plasma.

The plasma surrounding the Rosetta spacecraft became more influenced by the environment of the comet upon approach. Our goal

is to detect variations in the surrounding plasma as this happens, and get qualitative estimates about whether we collect hot or cold electrons. In order to ensure that equation (A6) is satisfied for cold electrons we take, as shown in Fig. 2, the current at the point $V_p = -10\,V$. Compensating for the acceleration and deceleration of the electrons due to $V_{s/c}$, we arrive at the condition $V_p = -10\,V + V_k$. To compare contributions from cold electrons and hotter electrons, we take the current at the point $V_p = -20\,V + V_k$. This method is limited by the range of bias potentials accessible for the different operational sweep modes, especially for the mode with the range [−12, 12] V, hence, the choice of not taking an even more negative potential to compare hot and cold electron contributions.

In order to get a complete picture of the surrounding plasma, we also investigate electron current fluctuations where $V_p > 0\,V$. As $V_{s/c}$ becomes very negative during the approach to the comet (e.g. Odelstad et al. 2015), the electron saturation current is, as mentioned above, often out of range, preventing us to do the same analysis as for the current where $V_p < 0\,V$. We take the current of the *I–V* curve for a fixed $V_p > 0$. We chose $V_p = 7V$ since it co-varies with the current at $V_p = 9V$ (when it is in range), suggesting that the photoelectron emission contributions can be neglected in this bias potential range.

This paper has been typeset from a TEX/LATEX file prepared by the author.